

# Hyperspectral Image Generation with Unmixing Guided Diffusion Model

Shiyu Shen, Bin Pan, Ziye Zhang and Zhenwei Shi

**Abstract**—Recently, hyperspectral image generation has received increasing attention, but existing generative models rely on conditional generation schemes, which limits the diversity of generated images. Diffusion models are popular for their ability to generate high-quality samples, but adapting these models from RGB to hyperspectral data presents the challenge of high dimensionality and physical constraints. To address these challenges, we propose a novel diffusion model guided by hyperspectral unmixing. Our model comprises two key modules: an unmixing autoencoder module and an abundance diffusion module. The unmixing autoencoder module leverages unmixing guidance to shift the generative task from the image space to the low-dimensional abundance space, significantly reducing computational complexity while preserving high fidelity. The abundance diffusion module generates samples that satisfy the constraints of non-negativity and unity, ensuring the physical consistency of the reconstructed HSIs. Additionally, we introduce two evaluation metrics tailored to hyperspectral data. Empirical results, evaluated using both traditional metrics and our proposed metrics, indicate that our model is capable of generating high-quality and diverse hyperspectral images, offering an advancement in hyperspectral data generation.

**Index Terms**—Hyperspectral Image Generation, Hyperspectral Unmixing, Diffusion Model.

## I. INTRODUCTION

**H**YPERSPECTRAL image (HSI) generation represents a critical need in remote sensing. HSI is significant in various applications [1], [2], but the acquisition of high-fidelity HSIs is constrained by limitations in sensor technology [3]. These challenges lead to the scarcity of large-scale, high-quality HSI data, hindering the advancements in hyperspectral research [4]. Consequently, synthesizing diverse HSIs has emerged as a pivotal yet underexplored task.

However, existing methods cannot expand data due to their conditional generation frameworks [5]. These approaches typically employ conditional constraints, such as RGB images or segmentation maps, to guide the distribution of generated hyperspectral images [6], [7]. While effective for spectral super-resolution, these methods fall short of generative modeling, as they prioritize spectral restoration over the comprehensive

The work was supported by the National Key Research and Development Program of China under Grant 2022YFA1003800, the National Natural Science Foundation of China under the Grant 62125102, and the Fundamental Research Funds for the Central Universities under grant 63243074. (Corresponding author: Bin Pan)

Shiyu Shen, Bin Pan (corresponding author) and Ziye Zhang are with the School of Statistics and Data Science, KLMDASR, LEBPS, and LPMC, Nankai University, Tianjin 300071, China (e-mail: shenshiyu@mail.nankai.edu.cn; panbin@nankai.edu.cn; zhangziye@mail.nankai.edu.cn).

Zhenwei Shi is with the Image Processing Center, School of Astronautics, Beihang University, Beijing 100191, China (e-mail: shitianyang@buaa.edu.cn; shizhenwei@buaa.edu.cn).

simulation of the underlying HSI distribution. Although conditional frameworks ensure high-fidelity outputs, they inherently limit the diversity of generated images.

Unconditional generation, while extensively explored for RGB images [8], [9], presents unique challenges when applied to HSIs:

- **High Dimensionality:** HSIs exhibit high spectral dimensionality, with hundreds of bands compared to the three bands in RGB images. This necessitates a fundamentally different model architecture compared to RGB generation models, which typically employ autoencoder structures [10], [11] to reduce spatial dimensions while enhancing spectral details.
- **Physical Constraints:** HSIs are governed by physical rules [12], [13], having limited unique spectral signatures compared to the diversity of RGB images. Rather than attempting to simulate the entire distribution indiscriminately, leveraging these constraints can enhance the fidelity and efficiency of HSI generation.

To address these challenges, we integrate hyperspectral unmixing into the generative framework. We project HSIs into the abundance space, which is low-dimensional and governed by the explicit constraints, namely non-negativity and unity [14]. By operating in the abundance space, a generative model can effectively synthesize hyperspectral data while maintaining physical consistency.

To implement the proposed framework, we introduce the Hyperspectral Unmixing Diffusion Model (HUD), which consists of two key components: an Unmixing AutoEncoder (UAE) pair and an Abundance Diffusion Module (ADM). To address the challenge of high dimensionality, we design the UAE module. UAE is initialized using a hyperspectral unmixing algorithm, where abundances are derived either through rigorously constrained optimization equations or a linear approximation. Reconstruction is performed directly using the endmembers, ensuring efficient dimensionality reduction while preserving essential spectral information. To address the challenge of physical constraint, we construct the ADM module. The diffusion model iteratively generates samples on the abundance space. However, traditional diffusion models rely on Gaussian distributions to describe latent features, which inherently violate the unity and non-negativity constraints of the abundance space. To address this limitation, we project the abundance space into an unconstrained domain, apply Gaussian-based sampling, and then map the generated samples back to the abundance space. This approach enables the generation of physically consistent and high-fidelity hyperspectral data while

maintaining computational efficiency. Moreover, we introduce two novel metrics tailored for HSI generation: point fidelity and block diversity. Experimental results indicate that HUD consistently outperforms existing models on both proposed metrics and traditional metrics.

Our contribution is summarized as the following:

- We develop a hyperspectral unmixing guided diffusion model for HSI generation.
- We propose an unmixing autoencoder module that shifts the generative task from the image space to the abundance space, reducing dimensionality while preserving fidelity.
- We propose an abundance diffusion module, which generates high-quality hyperspectral images that satisfy physical constraints.

The rest of this paper is organized as follows. In Section II, we review related works in the field. Section III provides a detailed description of the proposed model. In Section IV, we present the results of real-world experiments. Finally, we conclude the paper in Section V.

## II. RELATED WORK

In this section, we review diffusion models and existing methods for HSI generation. We also introduce the hyperspectral unmixing algorithm.

### A. Diffusion Models

Denoising Diffusion Probabilistic Models (DDPM) [15] have recently emerged as a hot topic in the field of generative networks. DDPM constructs a diffusion random process that gradually changes the image distribution into the standard Gaussian noise, and a denoising reverse process that changes the noise into an image. The denoising process is a Markov chain, and the transition probability is approximated by a U-Net [16].

Latent Diffusion Model [17], also known as Stable Diffusion, is an improvement of DDPM. The dimension of the intermediate variables during the denoising process of DDPM is constant. As a result, DDPM is faced with the problem of high computational expense and low image resolution. Stable diffusion encodes the original image into low-dimensional latent space and constructs a DDPM on it. The autoencoder is pretrained on ImageNet or other large-scale RGB datasets.

### B. HSI Generation

Existing methods for HSI generation typically rely on conditional images [18], [19]. Depending on the type of conditional input, HSI generation can be categorized into two main approaches: spectral super-resolution [20], [21], [22] which uses RGB or multi-spectral images as conditions, and synthesis based on semantic segmentation maps [23], [24]. A key challenge in HSI generation is the high spectral dimensionality, which differentiates hyperspectral images from RGB images. Regardless of the specific approach, most existing methods for HSI generation focus on generating individual pixels rather than full images. In these models, spatial distribution is conditioned on the input images, while

the primary task is the generation of the spectral content for each pixel.

Recently, several studies have explored the use of generative models for HSI generation, including GAN, VAE, and Stable Diffusion [25], [26], [27], [28], [29]. However, most of these approaches still rely on conditional images such as RGB or multi-spectral images during the generation process. This reliance limits the diversity of the generated hyperspectral images, as the spatial distribution is largely determined by the conditional input.

### C. Hyperspectral Unmixing

Hyperspectral unmixing assumes that a HSI can be modeled as a combination of endmembers and their corresponding abundances [14], [30], [31]. The fundamental assumption is described by the linear mixing model:

$$Y = AX + \varepsilon, \quad (1)$$

where  $Y \in R^{c \times h \times w}$  represents the HSI of spatial shape  $h \times w$  and spectral shape  $c$ ,  $A \in R^{c \times d}$  is the endmember matrix and  $d$  is the number of endmembers,  $X \in R^{d \times h \times w}$  is the abundance matrix, and  $\varepsilon$  is the residual noise. The goal of hyperspectral unmixing is to recover the matrices  $A$  and  $X$  based on  $Y$ , subject to physical constraints.

Recent advancements in hyperspectral unmixing have expanded beyond classical linear models to address complex spectral interactions and nonlinear mixing. Early geometric methods, such as Vertex Component Analysis (VCA) [32], identify endmembers by exploiting spectral data geometry. Statistical approaches like Nonnegative Matrix Factorization [14], [33], [34] enforce physical constraints during decomposition. Sparse unmixing frameworks [35], [36] leverage sparsity assumptions to improve interpretability. More recently, deep learning-based methods [37], [38], [39] have gained prominence, using neural networks to model nonlinear mixing and enhance accuracy under challenging conditions.

## III. METHOD

In this section, we show the detailed design of the proposed model, including the unmixing autoencoder module and the abundance diffusion module. We also introduce the evaluation metrics for hyperspectral image generation. The overall structure of HUD is shown in Figure 1.

### A. Unmixing Autoencoder Module

The unmixing autoencoder can use any algorithm to extract endmember, and in this paper we use VCA for example. Generally, abundance is typically subject to two key constraints: non-negativity and unity. Specifically, the abundance values for each pixel must be non-negative and sum to one, reflecting the physical interpretation that each pixel is composed of a mixture of endmembers in varying proportions. Therefore, given  $Y$  and  $A$ ,  $X$  is usually solved through a constrained optimization problem of the following form:

$$\min ||Y - AX||^2 \text{ s.t. } X \geq 0 \text{ and } \sum_i X_{(i,:,:)} = \mathbb{1}_{h \times w} \quad (2)$$

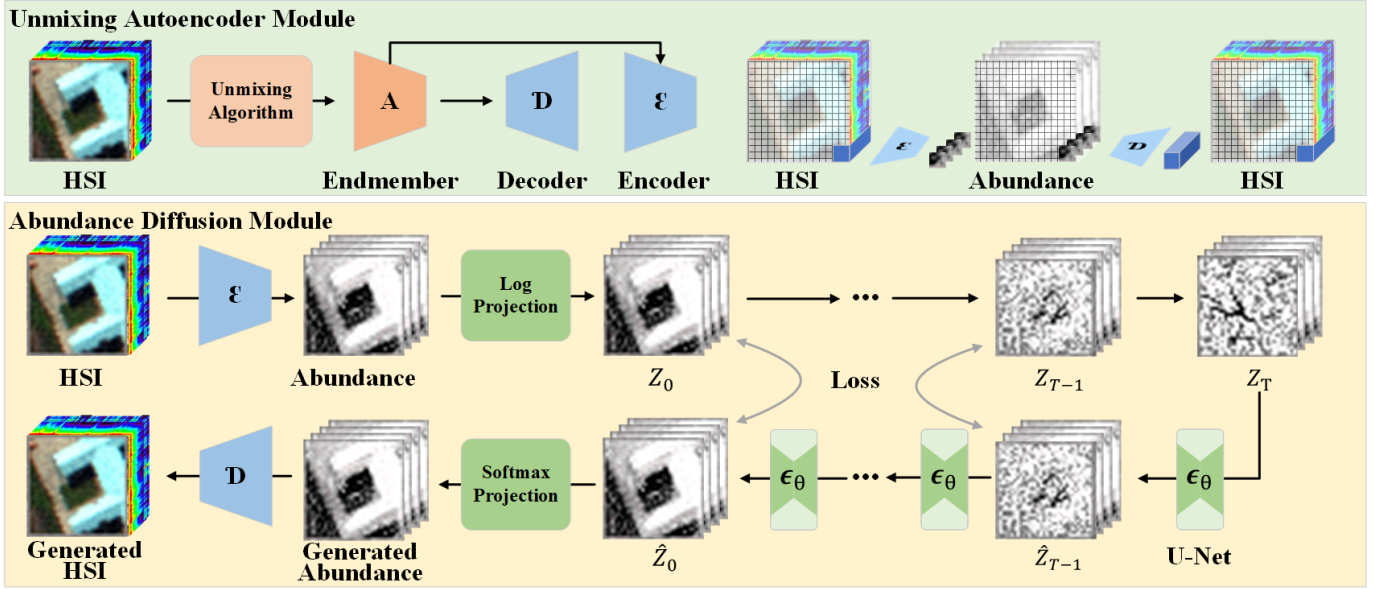


Fig. 1: Components of HUD. HUD is composed of 2 modules: the unmixing autoencoder and the abundance diffusion model.

In addition to the rigorous solution, a linear approximation can also be employed to solve for  $X$ . During the extraction of endmembers, many unmixing algorithms inherently incorporate constraints on abundance. As a result, even if these constraints are temporarily relaxed to solve for  $X$ , the approximate solution remains close to the rigorously constrained one. The linear approximation to this optimization problem can be expressed as:

$$X = (A^T A)^{-1} A^T Y. \quad (3)$$

This approximation provides a computationally efficient alternative while maintaining reasonable accuracy, making it suitable for scenarios where computational efficiency is prioritized.

To reconstruct the HSI, we employ a linear projection  $\hat{Y} = AX$ , where  $\hat{Y}$  represents the reconstructed HSI. In the proposed model, we initialize a linear layer as the decoder using the endmember matrix  $A$ , while the encoder is initialized as  $(A^T A)^{-1} A^T$ . This initialization can be based on either the linear approximation or the rigorous solution, depending on the desired balance between computational efficiency and accuracy. Although the autoencoder can be further optimized through data-driven training, the limited volume of HSI datasets increases the risk of severe overfitting. Therefore, we recommend using a frozen autoencoder in most scenarios, with fine-tuning reserved for cases where sufficient data is available to ensure robust training without compromising generalization. This approach balances computational efficiency, physical consistency, and the practical constraints of HSI data availability.

### B. Abundance Diffusion Module

We establish a diffusion module on the abundance space. The diffusion module approximates a Markov chain from a Gaussian distribution to the abundance distribution using a U-Net model. It consists of two processes: the diffusion process

from the abundance distribution to the Gaussian distribution and the denoising process from the Gaussian distribution to the abundance distribution.

Before training the diffusion model, we introduce a pair of differentiable projections to relax the constraints of non-negativity and unity imposed on the abundance maps. The projections are defined as follows:

$$Z[i, j, k] = \ln \left( X[i, j, k] + e^{-\ln(d)-8} \right), \quad (4)$$

$$\hat{X}[i, j, k] = \frac{e^{Z[i, j, k]}}{\sum_{i=1}^d e^{Z[i, j, k]}}, \quad (5)$$

where  $Z$  represents the projected feature in an unconstrained space, and  $\hat{X}$  is the reconstructed abundance map that satisfies the original constraints. This projection is designed to be lossy, with the difference between  $X$  and  $\hat{X}$  being negligible:

$$\hat{X}[i, j, k] = \frac{X[i, j, k] + e^{-\ln(d)-8}}{1 + e^{-8}}. \quad (6)$$

By operating on  $Z$  instead of  $X$ , the constraints are effectively relaxed during the diffusion process, while the final reconstruction  $\hat{X}$  still satisfies the non-negativity and unity conditions. The term  $e^{-\ln(d)-8}$  is added to avoid numerical instability caused by  $\ln(0)$ . Since the projection pair is fully differentiable, it can be seamlessly integrated into the end-to-end training of the diffusion model, enabling efficient optimization while preserving the physical consistency of the generated hyperspectral data.

Assume that the distribution of the projected abundance is  $Z_0 \sim q(Z_0)$ , the diffusion process is fixed to a Markov chain

that gradually adds Gaussian noise to the  $Z_0$  according to a variance schedule  $\beta_1, \beta_2, \dots, \beta_T$ :

$$q(Z_{1:T}|Z_0) := \prod_{t=1}^T q(Z_t|Z_{t-1}), \quad (7)$$

$$q(Z_t|Z_{t-1}) := \mathcal{N}(Z_t; \sqrt{1-\beta_t}Z_{t-1}, \beta_t\mathbf{I}) \quad (8)$$

The denoising process is the reverse of the diffusion process. The transition is a Gaussian distribution with learnable parameter  $\theta$ , which starts from  $p(Z_T) = \mathcal{N}(Z_T; (0), \mathbf{I})$ :

$$p_\theta(Z_{0:T}) := p(X_T) \prod_{t=1}^T p_\theta(Z_{t-1}|Z_t), \quad (9)$$

$$p_\theta(Z_{t-1}|Z_t) := \mathcal{N}(Z_{t-1}; \mu_\theta(Z_t, t), \Sigma_\theta(Z_t, t)) \quad (10)$$

To train the learnable distribution, we optimize a variational lower bound on the negative log-likelihood. Specifically, we aim to minimize the following objective:

$$\begin{aligned} \mathbf{E}[-\log p_\theta(Z_0)] &\leq \mathbf{E}_q \left[ -\log \frac{p_\theta(Z_{0:T})}{q(Z_{1:T}|Z_0)} \right] \\ &= \mathbf{E}_q \left[ -\log p(Z_T) - \sum_{t=1}^T \frac{p_\theta(Z_{t-1}|Z_t)}{q(Z_t|Z_{t-1})} \right] \end{aligned} \quad (11)$$

By notation  $\alpha_t := 1 - \beta_t$  and  $\bar{\alpha}_t := \prod_{s=1}^t \alpha_s$ , the loss term can be rewritten as:

$$\begin{aligned} \mathbf{E}_q[D_{KL}(q(Z_T|Z_0)||p(Z_T)) \\ + \sum_{t=2}^T D_{KL}(q(Z_{t-1}|Z_t, Z_0)||p_\theta(Z_{t-1}|Z_t)) \\ - \log p_\theta(Z_0|Z_1)] \end{aligned} \quad (12)$$

where

$$\begin{aligned} q(Z_t|Z_0) &= \mathcal{N}(Z_t; \sqrt{\bar{\alpha}_t}Z_0, (1-\bar{\alpha}_t)\mathbf{I}), \\ q(Z_{t-1}|Z_t, Z_0) &= \mathcal{N}(Z_{t-1}; \tilde{\mu}_t(Z_t, Z_0), \tilde{\beta}_t\mathbf{I}), \\ \tilde{\mu}_t(Z_t, Z_0) &= \frac{\sqrt{\bar{\alpha}_{t-1}}\beta_t}{1-\bar{\alpha}_t}Z_0 + \frac{\sqrt{\bar{\alpha}_t}(1-\bar{\alpha}_{t-1})}{1-\bar{\alpha}_t}Z_t, \\ \tilde{\beta}_t &= \frac{1-\bar{\alpha}_{t-1}}{1-\bar{\alpha}_t}\beta_t. \end{aligned}$$

For simplification, we assume that  $\Sigma_\theta(Z_t, t) = \sigma_t^2\mathbf{I}$ , and use reparameterizing  $Z_t(Z_0, \epsilon) = \sqrt{\bar{\alpha}_t}Z_0 = \sqrt{1-\bar{\alpha}_t}\epsilon$  for  $\epsilon \sim \mathcal{N}(0, \mathbf{I})$ , the middle term in Equation (12) can be written as:

$$\begin{aligned} D_{KL}(q(Z_{t-1}|Z_t, Z_0)||p_\theta(Z_{t-1}|Z_t)) \\ = \mathbb{E}_q \left[ \frac{1}{2\sigma_t^2} \|\tilde{\mu}_t(Z_t, Z_0) - \mu_\theta(Z_t, t)\|^2 \right] + C \\ = \mathbb{E}_{Z_0, \epsilon} \left[ \frac{1}{2\sigma_t^2} \left\| \frac{1}{\sqrt{\bar{\alpha}_t}}(Z_t(Z_0, \epsilon) - \frac{\beta_t}{\sqrt{1-\bar{\alpha}_t}}\epsilon) - \mu_\theta(Z_t(Z_0, \epsilon), t) \right\|^2 \right] \end{aligned} \quad (13)$$

As a result,  $\mu_\theta$  should approximate  $\frac{1}{\sqrt{\bar{\alpha}_t}}(Z_t - \frac{\beta_t}{\sqrt{1-\bar{\alpha}_t}}\epsilon)$ , so we choose the form of  $\mu_\theta$  as:

$$\mu_\theta(Z_t, t) = \frac{1}{\sqrt{\bar{\alpha}_t}}(Z_t - \frac{\beta_t}{\sqrt{1-\bar{\alpha}_t}}\epsilon_\theta(Z_t, t)) \quad (14)$$

where  $\epsilon_\theta$  is represented by a U-Net. Finally, the practical loss function is:

$$L := \mathbf{E}_{t, Z_0, \epsilon} \left[ \|\epsilon - \epsilon_\theta(\sqrt{\bar{\alpha}_t}Z_0 + \sqrt{1-\bar{\alpha}_t}\epsilon, t)\|^2 \right] \quad (15)$$

where  $t$  is uniformly distributed on  $[1 : T]$ .

After training, we sample from standard Gaussian distribution to get  $Z_T$  and follow the denoising process step by step. The training and sampling procedure are shown in Algorithms 1 and 2.

---

**Algorithm 1** Training

---

```

while not converged do
    sample minibatch  $Y$ 
     $X = \mathcal{E}(Y)$ 
     $Z_0 = \ln(X + e^{-\ln(d)-8})$ 
    sample  $t \sim \mathcal{U}[1 : T]$ 
    sample  $\epsilon \sim \mathcal{N}(0, \mathbf{I})$ 
    make backward propagation by  $\nabla_\theta \|\epsilon - \epsilon_\theta(\sqrt{\bar{\alpha}_t}Z_0 + \sqrt{1-\bar{\alpha}_t}\epsilon, t)\|^2$ 
end while

```

---

**Algorithm 2** Sampling

---

```

sample  $Z_T \sim \mathcal{N}(0, \mathbf{I})$ 
for  $t$  in  $T, T-1, \dots, 1$  do
    sample  $\epsilon \sim \mathcal{N}(0, \mathbf{I})$ 
     $Z_{t-1} = \frac{1}{\sqrt{\alpha_t}}(Z_t) - \frac{1-\alpha_t}{\sqrt{1-\alpha_t}}\epsilon_\theta(Z_t, t) + \sigma_t\epsilon$ 
end for
 $\hat{X} = \text{softmax}(Z_0)$ 
 $\hat{Y} = \mathcal{D}(\hat{X})$ 
return  $\hat{Y}$ 

```

---

### C. Point Fidelity and Block Diversity

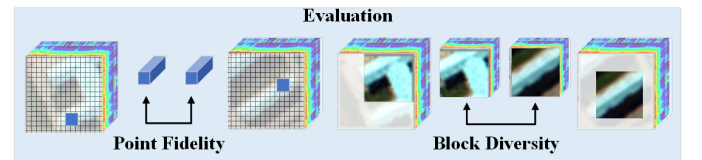


Fig. 2: Point fidelity and block diversity

Existing evaluation metrics for conditional HSI generation primarily focus on measuring the similarity between generated images and ground truth images, which are less effective for assessing the diversity and realism of the unconditionally generated samples. Inception Score (IS) and Fréchet Inception Distance (FID) are common choices in RGB image generation. However, they require a classification model pretrained on large-scale datasets, which is not feasible for HSI due to the limited data size. Moreover, IS and FID are not designed to capture the unique characteristics of HSI data, such as the high spectral dimensionality and limited spatial resolution.

Consequently, we propose two evaluation metrics tailored for HSI: point fidelity  $F_p$  and block diversity  $D_b$ . Point fidelity considers every pixel in the generated image and measures

the cosine similarity to the most similar pixel in the original image. To be specific:

$$F_p = \frac{1}{|\hat{Y}|} \sum_{\hat{y} \in \hat{Y}} \max_{y \in Y} \left[ \frac{\hat{y}}{\|\hat{y}\|} * \frac{y}{\|y\|} \right] \quad (16)$$

where  $Y$  is the real HSI,  $\hat{Y}$  is the generated HSI,  $y$  and  $\hat{y}$  are pixels, and  $|\hat{Y}|$  is the amount of pixels. In contrast, block diversity reflects whether the overall distribution of the generated HSI is a direct copy of the original HSI, or if there are differences in the distribution during the generation process. To be specific:

$$D_b = \frac{1}{N_b} \sum_{\hat{y}_b \in \hat{Y}} \frac{1}{\|\hat{y}_b\|} \max_{y_b \in X} \left[ \frac{\hat{y}_b}{\|\hat{y}_b\|} * \frac{y_b}{\|y_b\|} \right] \quad (17)$$

where  $N_b$  is the number of blocks,  $y_b$  is a block from the real HSI,  $\hat{y}_b$  is a block from the generated HSI. We assume that the generated image size is smaller than the original image because generating a full-sized hyperspectral image in the entire spatial domain is currently infeasible, even with reduced computational demand from the autoencoder.

#### IV. EXPERIMENTS

In this section, we empirically demonstrate the superiority of HUD. We first introduce the datasets used in the experiments, the comparison models, and the selection of hyperparameters. Then, we list images generated by different models. Finally, we analyze the performance of different models using quantitative metrics.

##### A. Experiments Setup

We use Indianpines, KSC, Pavia, PaviaU, and Salinas to showcase the generation results. (1) *Indianpines* contains an image scene with spatial size  $145 \times 145$  and 220 bands, covering a wavelength range of  $[104 - 108], [150 - 163], 220$  nm, having 16 classes. The Band 46,17,11 from the data are chosen for pseudo-color visualization. (2) *KSC* contains an image scene with spatial size  $512 \times 614$  and 176 bands, covering a wavelength range of 400 - 2500 nm, having 13 classes. The Band 28,9,10 from the data are chosen for pseudo-color visualization. (3) *Pavia* contains an image scene with spatial size  $1093 \times 715$  and 102 bands, having 9 classes. The Band 46,27,10 from the data are chosen for pseudo-color visualization. (4) *PaviaU* contains an image scene with spatial size  $610 \times 340$  and 103 bands, having 9 classes. The Band 46,27,10 from the data are chosen for pseudo-color visualization. (5) *Salinas* contains an image scene with spatial size  $512 \times 217$  and 204 bands, covering a wavelength range of  $[104 - 108], [150 - 163], 220$  nm, having 16 classes. The Band 36,17,11 from the data are chosen for pseudo-color visualization.

HUD will be compared with the following models: VAE, GAN [40], and MPRNet [41]. As there are currently no unconditional hyperspectral image generation algorithms, we adapted the classic models VAE and GAN from RGB generation tasks. Their first convolutional layer, usually a  $1 \times 1$  conv layer, is resized according to the dimensions of the dataset. The other

structures remain unchanged. We also evaluate the generation performance of MPRNet, a state-of-the-art hyperspectral image generation model, but it requires RGB images as conditions. Following the original paper, we directly input the pseudo RGB images to MPRNet.

The UAE of HUD is initialized separately for each dataset, and the dimensionality of  $Z$  is determined by the number of categories in the dataset. The UAE is pretrained and does not participate in the training of the diffusion model. The time steps of the diffusion model are set to 1000. Except for the downsampling layer, the structures and hyperparameters of VAE, GAN, and MPRNet are set according to the original papers.

All models are trained on a 4090 GPU. Although we designed the UAE to reduce the computational load of HUD, it still cannot generate full-sized hyperspectral images. Additionally, the comparison algorithms also fail to generate complete images. Therefore, during training, we randomly crop  $32 \times 32$  overlapping sub-images from the original image as training samples, and the generation process also produces  $32 \times 32$  images.

##### B. Qualitative Experiments

In this section, we will showcase the quality of generated images through visualization, including pseudo-color visualization and spectral curve visualization.

1) *Results on Pseudo-Color Images:* The pseudo-color visualization of 5 datasets is shown in Figure 3. The first column shows the pseudo-color visualization of the real HSI, and the generated images from different methods are listed on the right side. The pseudo-color visualization can reflect the spatial distribution of HSIs. Specifically, the generated images from GAN have grids overlay on the surface, resembling a mosaic. This problem is probability caused by the downsampling layers in generators and discriminators, which overlook some specific areas because of the pooling or striding operation. VAE directly estimates the distribution of original images, but the scheme limits the performance of the model. Consequently, the generated images from VAE are blurry and lack details. As a spectral super-resolution model, MPRNet generates images with high quality, but the spatial distribution is limited to the original image. HUD also generates high-quality images, and the spatial distribution is more diverse than MPRNet. For example, there are some new roads and buildings in the generated images of HUD, which are not present in the original images.

2) *Results on Spectral Curves:* The spectral curve distributions of the real HSI and the generated HSI are shown in Figure 4. We stack all the spectral curves of an HSI to show the spectral distributions. The boundary shows whether the generated spectral curves are consistent with the real HSI, and the density (color) infers the distribution of endmembers. Generally, GAN, MPRNet and HUD generate spectral curves that are more consistent with the real HSI than VAE. GAN tends to generate spectral curves that are frequently seen in the real HSI to confuse the discriminator by high-quality samples, so the distribution of generated spectral curves are concentrated. VAE only estimates the main characteristics of the real HSI

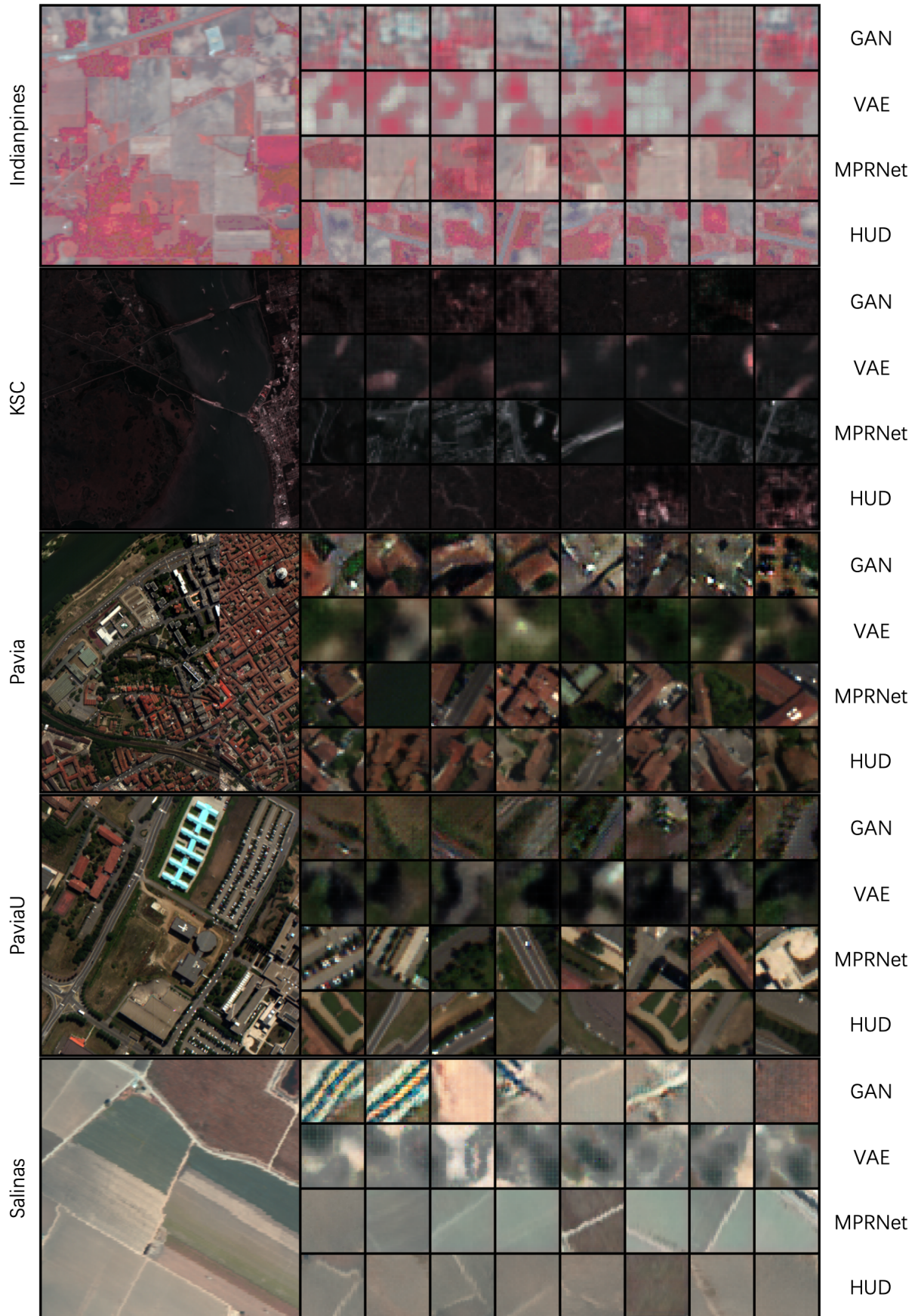


Fig. 3: Pseudo-color visualization of real HSI and generated HSI.

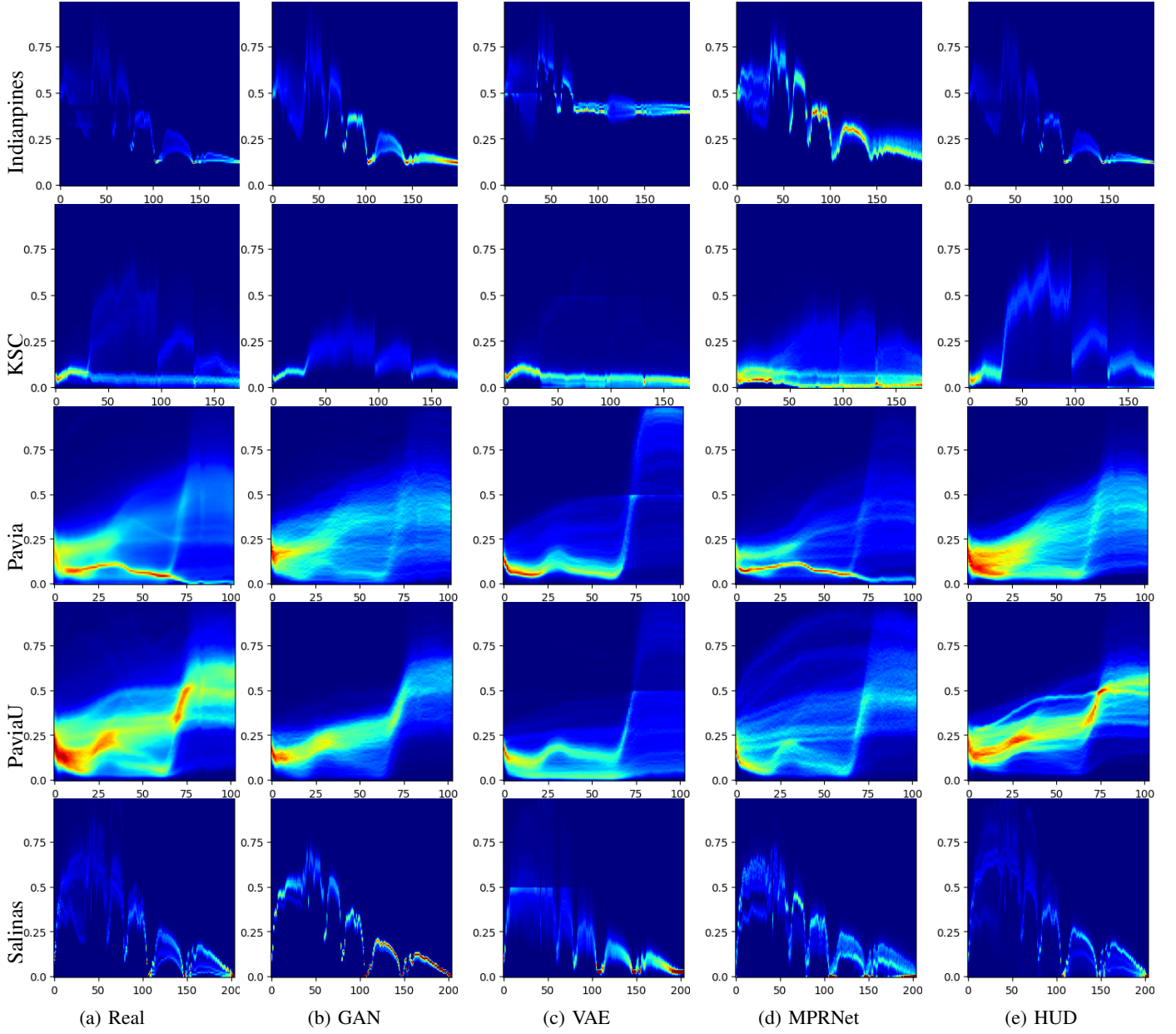


Fig. 4: Spectral curve distributions of real HSI and generated HSI.

due to the deficient structure. MPRNet generates high-quality spectral curves, but the distribution is limited to the real HSI, so the generated images lack diversity. HUD generates high-quality spectral curves that follows the overall shape and distribution of the real HSI, while there are also different distributions in the detail.

### C. Quantitative Experiments

In this section, we will quantitatively analyze the quality of generated images. The evaluation metrics include common IS and FID used in RGB generation tasks, as well as the proposed point fidelity and region diversity. We trained a classification network on each dataset to replace the ImageNet pretrained InceptionV3 used in calculating IS and FID.

*1) Results on Fidelity and Diversity:* The quantitative results are shown in Tables I to III. According to Table II, all models achieve similar results while HUD performs slightly better than the other models. According to Table III, the results are unstable across different datasets and models. IS and FID are originally proposed for RGB images, which requires a generally pretrained InceptionV3. However, the hyperspectral images have significant differences in distribution, so the classification networks should be trained on each dataset. As a result, the metrics are unstable and questionable. Regardless, HUD and GAN achieve the top results in the IS and FID comparison.

As shown in Table I, HUD achieves the highest point fidelity, indicating that its generated images better preserve the spectral content of real images. MPRNet, a spectral super-resolution model, ranks second in point fidelity. In terms of block

TABLE I: Point Fidelity and Block Diversity Comparison.

Dataset	$F_p \uparrow$				$D_b \downarrow$				$D_b/F_p \downarrow$			
	GAN	VAE	MPRNet	HUD	GAN	VAE	MPRNet	HUD	GAN	VAE	MPRNet	HUD
Indianpines	0.998	0.914	0.996	<b>0.999</b>	0.981	<b>0.914</b>	0.995	0.986	<b>0.983</b>	1.000	0.999	0.987
KSC	0.998	0.978	0.983	<b>0.999</b>	<b>0.976</b>	0.978	0.983	0.990	<b>0.988</b>	1.000	1.000	0.991
Pavia	0.996	0.941	<b>0.999</b>	<b>0.999</b>	0.949	0.936	0.942	<b>0.912</b>	0.953	0.995	0.943	<b>0.913</b>
PaviaU	0.996	0.941	0.997	<b>0.999</b>	0.948	0.934	0.984	<b>0.919</b>	0.952	0.992	0.987	<b>0.920</b>
Salinas	0.995	0.998	0.998	<b>0.999</b>	0.984	0.982	0.988	<b>0.981</b>	0.989	0.984	0.990	<b>0.982</b>
Avg	0.994	0.954	0.995	<b>0.999</b>	0.968	<b>0.949</b>	0.978	0.958	0.969	0.994	0.984	<b>0.959</b>

TABLE II: Inception Score Comparison.

Metric	Dataset	GAN	VAE	MPRNet	HUD
IS $\uparrow$	Indianpines	<b>1.08</b>	1.02	1.04	1.07
	KSC	1.00	1.00	1.00	1.00
	Pavia	1.01	1.01	<b>1.04</b>	1.01
	PaviaU	1.03	1.03	1.04	<b>1.05</b>
	Salinas	<b>1.05</b>	1.04	1.00	<b>1.05</b>
	Avg	1.03	1.02	1.03	<b>1.04</b>

TABLE III: Fréchet Inception Distance Comparison.

Metric	Dataset	GAN	VAE	MPRNet	HUD
FID $\downarrow$	Indianpines	8.03	240.91	20.98	<b>4.71</b>
	KSC	10.87	5.45	<b>4.76</b>	6.69
	Pavia	4.81	13.82	<b>2.37</b>	4.79
	PaviaU	4.92	9.13	3.13	<b>2.81</b>
	Salinas	<b>15.03</b>	21.33	29.09	23.12
	Avg	8.73	58.13	12.07	<b>8.42</b>

diversity, VAE generates the most diverse images, but its poor image quality results in lower point fidelity. HUD, however, achieves the best block diversity after VAE, demonstrating richer spatial distributions. MPRNet ranks lowest in block diversity, suggesting its generated images are overly constrained by the original spatial patterns. Combining both point and block diversity, HUD delivers the best overall performance, followed by GAN. Despite VAE excelling in block diversity, its overall performance remains the weakest.

2) *Results on Computational Complexity*: Due to the high dimensionality of hyperspectral images, we designed an autoencoder with unmixing guidance to reduce the computational load of the diffusion model. Despite the efforts, we were only able to generate 32x32 hyperspectral images in our experiments. This section compares the computational costs of different models for generating Indianpines images, including a hypothetical estimate for DDPM. The results are summarized in Table IV.

TABLE IV: Computational Complexity.

Size	Metric	GAN	VAE	MPRNet	HUD	DDPM
32	Params GB	0.49	0.49	0.56	1.15	1.43
	Memory GB	1.67	1.81	1.97	3.35	72.22
	FLOPs $10^{11}$	0.19	0.20	0.22	46.75	1038.21
256	Params GB	0.49	0.49	0.56	1.15	1.43
	Memory GB	9.93	11.05	12.43	18.75	567.75
	FLOPs $10^{11}$	1.52	1.60	1.76	374.00	8305.68

Diffusion models require more parameters (about double of the others) due to the full U-Net structure used for predicting noisy samples, while other models, like GANs and VAEs, only use decoder structures. Training costs for GANs and VAEs are similar to HUD because both require additional components like a discriminator or encoder. MPRNet, as a spectral super-resolution model, is cheaper since it directly generates HSIs from RGB inputs. Memory costs follow a similar pattern, with diffusion models requiring more memory due to their larger feature dimensions and iterative denoising process. For larger images (e.g., 256x256), computational complexity rises significantly, with 24 GB of memory insufficient for training models with batch size 4.

## V. CONCLUSION AND DISCUSSION

This paper introduces an unconditional hyperspectral image generation model that achieves both high fidelity and diversity, addressing the high dimensionality and physical constraint challenges posed by hyperspectral data. To overcome these challenges, we propose a novel framework comprising a hyperspectral unmixing autoencoder pair, which projects the original HSI into a low-dimensional abundance space for efficient generation. Additionally, we design a diffusion module capable of generating high-quality samples while satisfying the physical constraints of non-negativity and unity. Furthermore, we introduce a new evaluation method specifically tailored to the characteristics of hyperspectral data, providing a more accurate assessment of generation quality. Experimental results demonstrate that our model outperforms existing methods, generating higher-quality HSIs and paving the way for future advancements in hyperspectral image generation research.

HUD makes full use of hyperspectral unmixing to guide the latent space of the diffusion model. However, constrained by the characteristics of HSI that have limited data and significant distribution differences, we do not recommend further training the unmixing-initialized autoencoder to avoid severe overfitting. Additionally, we can only train one model per image rather than generating different hyperspectral images from a unified diffusion model. Furthermore, despite the significant reduction in dimensionality achieved by unmixing guidance, it is still not feasible to generate complete high-resolution hyperspectral images in practice. To address these issues, our future work will focus on a different methodology that can generate images with different bands. Additionally, spatial compression is also under consideration.

## REFERENCES

[1] G. Wang, X. Zhang, Z. Peng, S. Tian, T. Zhang, X. Tang, and L. Jiao, "Oral: An observational learning paradigm for unsupervised hyperspectral change detection," *IEEE Transactions on Circuits and Systems for Video Technology*, pp. 1–1, 2025.

[2] M. Jin, C. Wang, and Y. Yuan, "Dual heterogeneous network for hyperspectral image classification," *IEEE Transactions on Circuits and Systems for Video Technology*, vol. 35, no. 3, pp. 2905–2917, 2025.

[3] Q. Li, Y. Yuan, X. Jia, and Q. Wang, "Dual-stage approach toward hyperspectral image super-resolution," *IEEE Transactions on Image Processing*, vol. 31, pp. 7252–7263, 2022.

[4] S. Chen, L. Zhang, and L. Zhang, "Cyclic cross-modality interaction for hyperspectral and multispectral image fusion," *IEEE Transactions on Circuits and Systems for Video Technology*, vol. 35, no. 1, pp. 741–753, 2025.

[5] J. He, Q. Yuan, J. Li, Y. Xiao, D. Liu, H. Shen, and L. Zhang, "Spectral Super-Resolution Meets Deep Learning: Achievements and Challenges," *Information Fusion*, vol. 97, p. 101812, 2023.

[6] J. Zhang, R. Su, Q. Fu, W. Ren, F. Heide, and Y. Nie, "A Survey on Computational Spectral Reconstruction Methods from RGB to Hyperspectral Imaging," *Scientific Reports*, vol. 12, no. 1, p. 11905, 2022.

[7] H. Wang, C. Wang, and Y. Yuan, "Asymmetric dual-direction quasi-recursive network for single hyperspectral image super-resolution," *IEEE Transactions on Circuits and Systems for Video Technology*, vol. 33, no. 11, pp. 6331–6346, 2023.

[8] Y. Li, H. Liu, Q. Wu, F. Mu, J. Yang, J. Gao, C. Li, and Y. J. Lee, "Gligen: Open-set grounded text-to-image generation," in *Proceedings of the IEEE/CVF conference on computer vision and pattern recognition*, 2023, pp. 22511–22521.

[9] J. Zhu, H. Ma, J. Chen, and J. Yuan, "High-Quality and Diverse Few-Shot Image Generation via Masked Discrimination," *IEEE Transactions on Image Processing*, vol. 33, pp. 2950–2965, 2024.

[10] D. P. Kingma, "Auto-Encoding Variational Bayes," *arXiv preprint arXiv:1312.6114*, 2013.

[11] P. Esser, R. Rombach, and B. Ommer, "Taming Transformers for High-Resolution Image Synthesis," in *Proceedings of the IEEE/CVF conference on computer vision and pattern recognition*, 2021, pp. 12873–12883.

[12] P. Liu, Y. Zhao, K. Feng, and S. G. Kong, "Physics-driven multispectral filter array pattern optimization and hyperspectral image reconstruction," *IEEE Transactions on Circuits and Systems for Video Technology*, vol. 34, no. 10, pp. 9528–9539, 2024.

[13] X. Fu, Y. Guo, M. Xu, and S. Jia, "Hyperspectral Image Denoising via Robust Subspace Estimation and Group Sparsity Constraint," *IEEE Transactions on Geoscience and Remote Sensing*, vol. 61, pp. 1–16, 2023.

[14] X.-R. Feng, H.-C. Li, R. Wang, Q. Du, X. Jia, and A. Plaza, "Hyperspectral Umixing Based on Nonnegative Matrix Factorization: A Comprehensive Review," *IEEE Journal of Selected Topics in Applied Earth Observations and Remote Sensing*, vol. 15, pp. 4414–4436, 2022.

[15] J. Ho, A. Jain, and P. Abbeel, "Denoising Diffusion Probabilistic Models," *Advances in neural information processing systems*, vol. 33, pp. 6840–6851, 2020.

[16] O. Ronneberger, P. Fischer, and T. Brox, "U-Net: Convolutional Networks for Biomedical Image Segmentation," in *Medical Image Computing and Computer-Assisted Intervention—MICCAI 2015: 18th International Conference, Munich, Germany, October 5–9, 2015, Proceedings, Part III* 18. Springer, 2015, pp. 234–241.

[17] R. Rombach, A. Blattmann, D. Lorenz, P. Esser, and B. Ommer, "High-Resolution Image Synthesis with Latent Diffusion Models," in *Proceedings of the IEEE/CVF Conference on Computer Vision and Pattern Recognition*, 2022, pp. 10684–10695.

[18] L. Liu, S. Lei, Z. Shi, N. Zhang, and X. Zhu, "Hyperspectral Remote Sensing Imagery Generation from RGB Images Based on Joint Discrimination," *IEEE Journal of Selected Topics in Applied Earth Observations and Remote Sensing*, vol. 14, pp. 7624–7636, 2021.

[19] X. Wang, J. Chen, Q. Wei, and C. Richard, "Hyperspectral image super-resolution via deep prior regularization with parameter estimation," *IEEE Transactions on Circuits and Systems for Video Technology*, vol. 32, no. 4, pp. 1708–1723, 2022.

[20] P. Wang, B. Bayram, and E. Sertel, "A Comprehensive Review on Deep Learning Based Remote Sensing Image Super-Resolution Methods," *Earth-Science Reviews*, vol. 232, p. 104110, 2022.

[21] L. Zhang, X. Luo, S. Li, and X. Shi, "R2H-CCD: Hyperspectral Imagery Generation from RGB Images Based on Conditional Cascade Diffusion Probabilistic Models," in *IGARSS 2023–2023 IEEE International Geoscience and Remote Sensing Symposium*. IEEE, 2023, pp. 7392–7395.

[22] R. Hang, Q. Liu, and Z. Li, "Spectral super-resolution network guided by intrinsic properties of hyperspectral imagery," *IEEE Transactions on Image Processing*, vol. 30, pp. 7256–7265, 2021.

[23] D. Wang, J. Zhang, B. Du, L. Zhang, and D. Tao, "DCN-T: Dual Context Network with Transformer for Hyperspectral Image Classification," *IEEE Transactions on Image Processing*, vol. 32, pp. 2536–2551, 2023.

[24] N. Chen, J. Yue, L. Fang, and S. Xia, "SpectralDiff: A Generative Framework for Hyperspectral Image Classification with Diffusion Models," *IEEE Transactions on Geoscience and Remote Sensing*, 2023.

[25] S. Hao, Y. Xia, and Y. Ye, "Generative Adversarial Network with Transformer for Hyperspectral Image Classification," *IEEE Geoscience and Remote Sensing Letters*, 2023.

[26] L. Pang, X. Cao, D. Tang, S. Xu, X. Bai, F. Zhou, and D. Meng, "HSIGENE: A Foundation Model for Hyperspectral Image Generation," *arXiv preprint arXiv:2409.12470*, 2024.

[27] L. Liu, B. Chen, H. Chen, Z. Zou, and Z. Shi, "Diverse Hyperspectral Remote Sensing Image Synthesis with Diffusion Models," *IEEE Transactions on Geoscience and Remote Sensing*, vol. 61, pp. 1–16, 2023.

[28] Y. Yu, E. Pan, Y. Ma, X. Mei, Q. Chen, and J. Ma, "UnmixDiff: Umixing-Based Diffusion Model for Hyperspectral Image Synthesis," *IEEE Transactions on Geoscience and Remote Sensing*, vol. 62, pp. 1–18, 2024.

[29] W. Liu, J. You, and J. Lee, "HSIGAN: A Conditional Hyperspectral Image Synthesis Method with Auxiliary Classifier," *IEEE Journal of Selected Topics in Applied Earth Observations and Remote Sensing*, vol. 14, pp. 3330–3344, 2021.

[30] J. M. Bioucas-Dias, A. Plaza, N. Dobigeon, M. Parente, Q. Du, P. Gader, and J. Chanussot, "Hyperspectral Umixing Overview: Geometrical, Statistical, and Sparse Regression-Based Approaches," *IEEE journal of selected topics in applied earth observations and remote sensing*, vol. 5, no. 2, pp. 354–379, 2012.

[31] R. A. Borsoi, T. Imbiriba, J. C. M. Bermudez, C. Richard, J. Chanussot, L. Drumetz, J.-Y. Tourneret, A. Zare, and C. Jutten, "Spectral Variability in Hyperspectral Data Umixing: A Comprehensive Review," *IEEE geoscience and remote sensing magazine*, vol. 9, no. 4, pp. 223–270, 2021.

[32] J. M. Nascimento and J. M. Dias, "Vertex Component Analysis: A Fast Algorithm to Unmix Hyperspectral Data," *IEEE Transactions on Geoscience and Remote Sensing*, vol. 43, no. 4, pp. 898–910, 2005.

[33] S. Zhang, G. Zhang, F. Li, C. Deng, S. Wang, A. Plaza, and J. Li, "Spectral-Spatial Hyperspectral Umixing Using Nonnegative Matrix Factorization," *IEEE Transactions on Geoscience and Remote Sensing*, vol. 60, pp. 1–13, 2022.

[34] M. Iftene, F. Z. Benhalouche, Y. K. Benkouider, and M. S. Karoui, "Partial NMF-Based Hyperspectral Unmixing Methods for Linear Mixing Models Addressing Intra-Class Variability," *Digital Signal Processing*, vol. 143, p. 104264, 2023.

[35] X. Shen, L. Chen, H. Liu, X. Su, W. Wei, X. Zhu, and X. Zhou, "Efficient hyperspectral sparse regression unmixing with multilayers," *IEEE Transactions on Geoscience and Remote Sensing*, vol. 61, pp. 1–14, 2023.

[36] B. Rasti and B. Koirala, "Suncnn: Sparse unmixing using unsupervised convolutional neural network," *IEEE Geoscience and Remote Sensing Letters*, vol. 19, pp. 1–5, 2021.

[37] X. Xu, X. Song, T. Li, Z. Shi, and B. Pan, "Deep Autoencoder for Hyperspectral Unmixing via Global-Local Smoothing," *IEEE Transactions on Geoscience and Remote Sensing*, vol. 60, pp. 1–16, 2022.

[38] Y. Gao, B. Pan, X. Xu, X. Song, and Z. Shi, "A Reversible Generative Network for Hyperspectral Umixing with Spectral Variability," *IEEE Transactions on Geoscience and Remote Sensing*, 2024.

[39] D. Hong, L. Gao, J. Yao, N. Yokoya, J. Chanussot, U. Heiden, and B. Zhang, "Endmember-Guided Umixing Network (EGU-Net): A General Deep Learning Framework for Self-Supervised Hyperspectral Umixing," *IEEE Transactions on Neural Networks and Learning Systems*, vol. 33, no. 11, pp. 6518–6531, 2022.

[40] I. Gulrajani, F. Ahmed, M. Arjovsky, V. Dumoulin, and A. C. Courville, "Improved Training of Wasserstein GANs," *Advances in neural information processing systems*, vol. 30, 2017.

[41] S. W. Zamir, A. Arora, S. Khan, M. Hayat, F. S. Khan, M.-H. Yang, and L. Shao, "Multi-Stage Progressive Image Restoration," in *Proceedings of the IEEE/CVF Conference on Computer Vision and Pattern Recognition (CVPR)*, June 2021, pp. 14821–14831.

**Shiyu Shen** received the B.S. degree from School of Mathematic Science, Nankai University, Tianjin, China, in 2021. He is currently working toward the Ph.D. degree in School of Statistics and Data Science, Nankai University. His research interests include machine learning, representation learning and uncertainty estimation.

**Bin Pan** received the B.S. and Ph.D. degrees from the School of Astronautics, Beihang University, Beijing, China, in 2013 and 2019, respectively. Since 2019, he has been an Associate Professor with School of Statistics and Data Science, Nankai University. His research interests include machine learning, remote sensing image processing and multi-objective optimization.

**Zifeng Yang** received the B.S. degree from Nankai University, Tianjin, China, in 2023. He is currently working toward the M.S. degree at the School of Statistics and Data Science, Nankai University. His research interests include machine learning, image generation, and diffusion models.

**Zhenwei Shi** received the Ph.D. degree in mathematics from the Dalian University of Technology, Dalian, China, in 2005. He was a Post-Doctoral Researcher with the Department of Automation, Tsinghua University, Beijing, China, from 2005 to 2007. He was a Visiting Scholar with the Department of Electrical Engineering and Computer Science, Northwestern University, Evanston, IL, USA, from 2013 to 2014. He is currently a Professor and the Dean of the Image Processing Center, School of Astronautics, Beihang University, Beijing. He has authored or coauthored over 200 scientific articles in refereed journals and proceedings, including the IEEE Transactions on Pattern Analysis and Machine Intelligence, the IEEE Transactions ON Image Processing, the IEEE Transactions on Geoscience and Remote Sensing, the IEEE Geoscience and Remote Sensing Letters, the IEEE Conference on Computer Vision and Pattern Recognition (CVPR), and the IEEE International Conference on Computer Vision (ICCV). His research interests include remote sensing image processing and analysis, computer vision, pattern recognition, and machine learning. Dr. Shi serves as an Editor for the IEEE Transactions on Geoscience and Remote Sensing, the Pattern Recognition, the ISPRS Journal of Photogrammetry and Remote Sensing, and the Infrared Physics and Technology. His personal website is <http://levir.buaa.edu.cn/>.